

# Journal of Medical Imaging

MedicalImaging.SPIEDigitalLibrary.org

## **Multiphysics modeling toward enhanced guidance in hepatic microwave ablation: a preliminary framework**

Jarrold A. Collins  
Jon S. Heiselman  
Logan W. Clements  
Daniel B. Brown  
Michael I. Miga

**SPIE.**

Jarrold A. Collins, Jon S. Heiselman, Logan W. Clements, Daniel B. Brown, Michael I. Miga, "Multiphysics modeling toward enhanced guidance in hepatic microwave ablation: a preliminary framework," *J. Med. Imag.* **6**(2), 025007 (2019), doi: 10.1117/1.JMI.6.2.025007.

# Multiphysics modeling toward enhanced guidance in hepatic microwave ablation: a preliminary framework

Jarrold A. Collins,<sup>a,\*</sup> Jon S. Heiselman,<sup>a</sup> Logan W. Clements,<sup>a</sup> Daniel B. Brown,<sup>b</sup> and Michael I. Miga<sup>a,b</sup>

<sup>a</sup>Vanderbilt University, Department of Biomedical Engineering, Nashville, Tennessee, United States

<sup>b</sup>Vanderbilt University Medical Center, Department of Radiology and Radiological Sciences, Nashville, Tennessee, United States

**Abstract.** We compare a surface-driven, model-based deformation correction method to a clinically relevant rigid registration approach within the application of image-guided microwave ablation for the purpose of demonstrating improved localization and antenna placement in a deformable hepatic phantom. Furthermore, we present preliminary computational modeling of microwave ablation integrated within the navigational environment to lay the groundwork for a more comprehensive procedural planning and guidance framework. To achieve this, we employ a simple, retrospective model of microwave ablation after registration, which allows a preliminary evaluation of the combined therapeutic and navigational framework. When driving registrations with full organ surface data (i.e., as could be available in a percutaneous procedure suite), the deformation correction method improved average ablation antenna registration error by 58.9% compared to rigid registration (i.e.,  $2.5 \pm 1.1$  mm,  $5.6 \pm 2.3$  mm of average target error for corrected and rigid registration, respectively) and on average improved volumetric overlap between the modeled and ground-truth ablation zones from  $67.0 \pm 11.8\%$  to  $85.6 \pm 5.0\%$  for rigid and corrected, respectively. Furthermore, when using sparse-surface data (i.e., as is available in an open surgical procedure), the deformation correction improved registration error by 38.3% and volumetric overlap from  $64.8 \pm 12.4\%$  to  $77.1 \pm 8.0\%$  for rigid and corrected, respectively. We demonstrate, in an initial phantom experiment, enhanced navigation in image-guided hepatic ablation procedures and identify a clear multiphysics pathway toward a more comprehensive thermal dose planning and deformation-corrected guidance framework. © 2019 Society of Photo-Optical Instrumentation Engineers (SPIE) [DOI: 10.1117/1.JMI.6.2.025007]

Keywords: deformation; image-guided surgery; microwave ablation; liver; registration.

Paper 18283R received Dec. 28, 2018; accepted for publication Apr. 23, 2019; published online May 20, 2019.

## 1 Introduction

### 1.1 Clinical Factors

Loco-regional therapies, such as thermal ablation, have received increased indications for use in neoadjuvant roles, ablation-assisted resection, and for the treatment of unresectable hepatic malignancies.<sup>1–8</sup> While radiofrequency ablation (RFA) is the most common ablative therapy used clinically, it has presented a relatively high local recurrence rate (12% to 39%) when compared to microwave ablation (MWA) (6% to 8.8%).<sup>1–5</sup> In addition, in matched cohort studies, patients receiving MWA saw improved survival compared to those receiving RFA.<sup>2,3</sup> Furthermore, MWA has received considerable interest due to its larger spatial extent of power deposition, penetration through charred tissues, and ability to ablate up to and around large vessels.<sup>2,3,7</sup> Due to advances in neoadjuvant care, therapeutic options, and improved patient selection criteria, the long-term survival of patients receiving ablation treatments for hepatic colorectal cancer metastases has improved significantly in recent years<sup>3,6,8</sup> and, in smaller tumors ( $\leq 3$  cm), is comparable to the clinical standard of surgical resection that can offer 5-year survival of 44% to 50% in patients with metastatic colorectal cancer.<sup>9</sup>

As the procedural process inherently targets internal structures, the efficacy of ablation is highly reliant on accurate localization and targeting of these subsurface lesions during a

procedure, as inaccurate delivery can lead to incomplete treatment and local recurrence.<sup>10</sup> As such, ablations are generally performed using image-guidance [e.g., intraoperative ultrasound imaging (iUS) or computed tomography (CT)] to assist in tumor localization and probe placement. However, with these methods, real-time localization, monitoring, and assessment are extremely limited. Further, these factors are delivery-mode dependent, as hepatic tumor ablation can be performed percutaneously, laparoscopically, or in open surgery.

Regarding clinical standards for ablation procedural planning, geometric estimates of expected ablation zone size and shape are provided by device manufacturers based on experimental measurements taken from *ex vivo* animal tissue. As such, these predictions ignore patient-specific anatomical and physiological variation, potential tissue heterogeneity, tissue perfusion, and differences in disease state that may be present. Accordingly, such estimates have been observed to often over-predict size and result in more homogeneous shapes when compared to clinical ablation outcomes.<sup>11,12</sup>

### 1.2 Localization and Therapy Guidance

Recent applications for image-guided ablation procedures have reported enhanced localization of tumors and improved accuracy of ablation antenna placement in open<sup>13–16</sup> and laparoscopic procedures.<sup>17–20</sup> These methods have employed a variety of electromagnetic (EM) tracking, optical tracking, and registration methods to provide enhanced image-guidance. However, to

\*Address all correspondence to Jarrod A. Collins, E-mail: [jarrod.a.collins@vanderbilt.edu](mailto:jarrod.a.collins@vanderbilt.edu)

date, image-guided ablation methods providing image-to-physical registration in open and laparoscopic settings have been limited to rigid registration approaches, which neglect soft-tissue deformations that occur from organ mobilization during these procedures and can cause substantial registration error.<sup>21</sup> EM-tracking, combined with iUS methods, attempts to circumvent this problem by tracking the real-time position of surgical tools in relation to real-time iUS imaging. However, the EM-iUS approach has limited information, can suffer from poor contrast, and loses efficacy when targeting lesions in cirrhotic patients or in those with chemotherapy-induced hyper-echogenicity associated with steatosis, both of which can compromise ultrasound lesion visualization.<sup>22,23</sup>

Several model-based soft-tissue deformation correction approaches have been presented in the literature for deformable image registration for hepatic resection. For example, Lange et al.<sup>24</sup> published an algorithm using thin-plate splines to deform preoperatively acquired vessels to intraoperative vessels acquired from tracked iUS. Hu et al.<sup>25</sup> presented a method using coherent point drift to nonrigidly register vessel landmarks, such as bifurcations. Alternatively, other approaches have concentrated on achieving surface-based deformation correction methods. Rucker et al.<sup>26</sup> described an inverse approach that optimizes boundary conditions described by a parameterized posterior displacement field, based on the reality of organ deformation during operative mobilization, to minimize the residual error between the intraoperatively collected anterior surface digitization and the deformed model surface. More recently, Heiselman et al.<sup>27</sup> expanded upon the work of Rucker et al. by reformulating the application of boundary conditions to a control point strategy, which allows for multiple independent support surfaces to be designated. Both surface-based methods have demonstrated effective correction of soft-tissue deformation in phantom and clinical applications for hepatic resection.<sup>26-30</sup>

With respect to thermal dose guidance, predictive, biophysical modeling of MWA presents a strong alternative to the manufacturer-provided estimates of ablation outcome by utilizing numerical approaches to solve the physical governing equations defining energy deposition and heat transfer. Other direct thermographic measurement strategies such as MR<sup>31</sup> and US<sup>32</sup> thermography are on the horizon, but these also have high technical and economic hurdles for practical use in the operating room or interventional suite. A computational approach driven by sparse data would certainly have some advantages. Recent modeling work has focused on treating tissue properties as a function of temperature.<sup>33-35</sup> These models were generally characterized within *ex vivo* animal tissue or simulation. Additional work is still needed to understand the variations that can present between patients due to differences in tissue properties<sup>32-35</sup> related to perfusion<sup>36-40</sup> or disease state (e.g., steatosis or cirrhosis<sup>41,42</sup>). Clearly, there is further need for prospective MWA modeling approaches. In addition, however, with respect to model-based solutions to guidance, there is certainly need of studying the power of integrating advanced surgical navigation methods with predictive MWA modeling in the delivery of ablation planning, delivery, and execution.

### 1.3 Impact for Surgical Open and Laparoscopic Procedures

When specifically considering the open and laparoscopic settings, as is the primary focus of this paper, advanced navigation approaches have been used to create a spatial mapping between

surgical instrumentation and imaging data to improve visualization of anatomical structures. Based on our existing image-guidance work for surgical resection,<sup>26-30</sup> the work here uses a hepatic deformation phantom setup designed to evaluate the accuracy of ablation probe localization when using the deformation correction method of Heiselman et al.<sup>27</sup> as compared to a clinically relevant rigid registration method.<sup>43</sup> With respect to presentation, only a portion of the anterior surface of the liver is available for organ-to-organ registration and assumes deformation conditions that are associated with surgical packing, i.e., the presented liver for surgery is first mobilized from the ligamenture, and then immobilized with surgical packing placed beneath the posterior surface of the organ. Careful attention has been paid such that the deformation patterns mimic those found in a previous clinical study of open resection by Clements et al.<sup>44</sup> Finally, as the impact of the work is considered, the performance evaluation clearly speaks to MWA ablation localization and prediction under conditions in open and laparoscopic surgery.

### 1.4 Impact for Percutaneous Procedures

Percutaneous image-guided ablation has become a powerful option in liver cancer patients not eligible for resection or waiting for transplant.<sup>45,46</sup> Due to its low complication rate, good efficacy, and minimally invasive nature, it is a common approach to control and manage liver cancer progression. However, when compared to resection or ablation in the open surgical setting, ablation site recurrence is quite high.<sup>47</sup> Improving percutaneous ablative procedures is an important need. In this work, while mock organ presentations that correlate with percutaneous delivery are not specifically considered, the framework was engaged in the context of organ-to-organ deformable registration with full liver surface availability. This would resemble conditions where x-ray-based technologies are being utilized for guidance such as with C-arm cone beam computed tomography (CBCT) systems. CBCT guidance for percutaneous ablation has shown improved effectiveness and safety in multiple studies.<sup>48-53</sup> However, studies evaluating image registration with CBCT for ablative treatment in the liver are limited and even more so with respect to the impact of deformations.<sup>50-53</sup> As a result, the experimental design herein was employed to establish results in the case where complete liver surface digitization is available. Yet, it is acknowledged that the percutaneous workflow, mode of soft-tissue deformation, and the dynamic nature of percutaneous intervention are not addressed.

## 2 Methods

### 2.1 Overview of Validation Study

In this study, a deformable hepatic phantom constructed of albumin suspended in agar was treated with 915 MHz MWA (ST antenna, Perseon, Salt Lake City, Utah) creating a visible ablation lesion. The ablated phantom was imaged using T<sub>2</sub>-weighted MRI, from which the phantom boundary, ablation zone, antenna tip, and antenna insertion point were segmented in the initial “predeformation” pose of the phantom. Next, support blocks were inserted beneath the phantom to change the underlying posterior support surface shape as well as to shift the ablation (e.g., similar to deformations observed in an open surgical setting<sup>26,44</sup>). The phantom was then reimaged in this

“postdeformation” state, providing the same information as before but in this new deformed pose. This two-step process effectively provided all procedural delivery information and ablation physical outcomes “before” and “after” a deforming event.

Image-to-physical registration was then performed by registering the initial predeformation image to the mock full-/sparse-surface digitization of the organ generated from the post-deformation imaging data. This experimental setup allowed the ablation information to effectively be used as a geometric target for registration assessment. In addition, a simple, retrospective model of the MWA procedure (i.e., a model of antenna power deposition and thermal distribution) was simulated in the pre-deformation pose given the antenna location segmented from MRI. We should note that the retrospective model was optimized to match the ablation measured. This was done to establish a baseline of the best possible outcome of model-to-physical ablation domain comparison as model error is inevitable. Together, these experiments allow the initial investigation of how well a computationally modeled, deformation-corrected ablation prediction performed versus the ground truth ablation extent and location (i.e., the evaluation of a model-based therapeutic and localization system). The experiment included a total of three ablations present in eight registration scenarios. To our knowledge, this combined evaluation is a unique contribution to the literature.

## 2.2 Summary of Image-to-Physical Registration Methods

Two methods of image-to-physical registration were evaluated in this study: a conventional rigid registration and a nonrigid registration approach that corrects for deformation. Rigid registration methods are currently the standard method used in commercial navigation systems. These methods are very fast, an essential requirement in the OR, but they rely on the assumption that the transformation from image-to-physical space is purely rigid and therefore could have poor behavior when deformation is present. The rigid registration method used in this study iteratively seeks to align the anterior organ surface and salient anatomical features in the predeformation image to the analogous sparse-surface and feature data designated in physical space. These data are synthesized from the postdeformation image data in this experiment, although in a typical clinical case, the sparse-surface and feature data would be collected by the physician in the operating room with an optically tracked stylus. Typical data collection involves the acquisition of three-dimensional (3-D) points over the anterior liver surface and specific features (falciform, round ligament, and inferior ridges). To mimic the quality of data available in a clinical setting, a sparse clinical collection pattern was taken of the anterior liver phantom surface in its postdeformation state. We should note that this distribution was extracted from the image volume data rather than acquired from conventional image-guidance instrumentation (details are in Sec. 2.7). With respect to the details of the rigid registration, these are described by Clements et al.<sup>43</sup> and their clinical efficacy have been reported in subsequent work.<sup>26–30</sup>

To better account for intraoperative deformations in the image alignment, the second method of registration evaluated in this study was a nonrigid, model-based approach designed to account for soft-tissue deformations. This deformable registration method seeks to minimize the difference between the

surface generated from the segmented image volume of the preoperative image and the sparse anterior surface data acquired in the mock intraoperative physical space. Briefly, the technique manipulates a set of surface control points distributed across the model surface in areas of anticipated deformation. Perturbations of the control points provide a precomputed distribution of volumetric displacements to the biomechanical model. Intraoperatively, optimization ensues iteratively with an active boundary condition reconstruction with simultaneous rigid parameter update until the preoperative organ shape matches the intraoperative counterpart. Optimization is performed using the Levenberg–Marquardt algorithm. The details of this method have been reported by Heiselman et al.<sup>27</sup>

## 2.3 Microwave Ablation Model

We utilize a two-dimensional axially symmetric computational model developed within COMSOL Multiphysics (COMSOL Inc, Burlington, Massachusetts) and Matlab 2017b (The Mathworks Inc., Natick, Massachusetts) to retrospectively model MWA with the 915-MHz Perseon short-tip (ST) antenna within an agar-albumin phantom. These retrospective models were then registered to their known locations in image space, simulating a preoperatively determined procedural plan. Following image-to-physical registration, we can then evaluate the accuracy of the registered ablation model when compared to the ground-truth ablation zone.

With respect to the biophysics, the electromagnetic wave equation was implemented to describe the propagation of electromagnetic waves through the mock soft-tissue phantom:

$$(\nabla^2 + \omega^2 \mu \epsilon_c) \vec{E} = 0, \quad (1)$$

where  $\omega$  (rad/s) is the angular frequency of the electromagnetic wave,  $\mu$  (H/m) is the permeability,  $\epsilon_c$  is the complex permittivity, and  $E$  (V/m) is the electric field strength. Penné’s bioheat transfer equation was employed to describe the temperature evolution and heat transfer:

$$\rho c \frac{\partial T}{\partial t} = \nabla \cdot k \nabla T + Q - Q_p, \quad (2)$$

where  $\rho$  (kg/m<sup>3</sup>) is the mass density,  $c$  (J/kg · K) is the specific heat capacity,  $k$  (W/m · K) is the thermal conductivity,  $T$  (K) is the instantaneous temperature,  $Q$  (W/m<sup>3</sup>) is the heat generation, and  $Q_p$  (W/m<sup>3</sup>) is the heat loss due to perfusion. Perfusion was not implemented within the phantom and as a result was excluded from the model. Heat generation within the phantom,  $Q$ , was modeled as a function of the rate of microwave energy absorption, as such:

$$Q = \frac{1}{2} \sigma \|E\|^2, \quad (3)$$

where  $\sigma$  (S/m) is the electrical conductivity.

An electromagnetic wave transparent boundary condition was applied at the outer edges of the modeling domain to prohibit microwave reflection:

$$\vec{n} \times (\nabla \times \vec{E}) - jk \vec{n} \times (\vec{E} \times \vec{n}) = 0, \quad (4)$$

where  $\vec{n}$  is the direction normal to the boundary and  $k$  is the wave number. The antenna is modeled as a conventional

conductive core surrounded by dielectric material, catheter, with ring-shaped slot cut on the outer conductor. Conductive material is not specifically realized but represented by the boundary condition:

$$\vec{n} \times \vec{E} = 0. \quad (5)$$

The microwave source itself is modeled as a port boundary condition, which relates the field to the square root of the time average power flow in the cable and is adopted from Ref. 54. This antenna model was consistent with observed performance; however, exact industry specifications were not available.

External boundaries were set to a fixed temperature (room temperature). Internal boundaries between the phantom and ablation antenna simulated saline cooling within the antenna with a convective heat flux condition:

$$\vec{n} \cdot (-k\nabla T) = h \cdot (T - T_{\text{ext}}), \quad (6)$$

where  $\vec{n}$  is the normal vector to the element,  $k$  (W/m · K) is the thermal conductivity,  $h$  (W/m<sup>2</sup> · K) is the heat transfer coefficient,  $T$  (K) is the temperature, and  $T_{\text{ext}}$  is the saline temperature (room temperature).

To simulate biological ablation, a mock cell necrosis was approximated as a function of protein denaturation and was estimated at each time step by the Arrhenius damage integral:

$$\alpha = \int_0^t A \exp\left[-\frac{E_a}{RT(t)}\right] dt, \quad (7)$$

where  $\alpha$  is the degree of damage at a given time,  $A$  (1/s) is a frequency factor,  $E_a$  (J/mol) is the activation energy required to denature the protein within the phantom,  $R$  (J/mol · K) is the universal gas constant, and  $T(t)$  (K) is the phantom temperature history. The estimated fraction of denatured protein was then calculated as

$$\theta_d = 1 - e^{-\alpha}. \quad (8)$$

## 2.4 Phantom Property Reconstruction

The model conveyed in Sec. 2.3 was retrospectively fit to ground truth data from mock gross pathology of our phantom from which ablation extent could be determined. The computational model fitting framework is based on a nonlinear optimization approach where a parameter set defining the dielectric and thermal properties of the phantom domain within the finite element model is iteratively chosen to maximize the overlap between the model-predicted and observed ablation zones:

$$P = [\sigma, \epsilon, k, c], \quad (9)$$

where  $\sigma$ ,  $\epsilon$ ,  $k$ , and  $c$  are the electrical conductivity, relative permittivity, thermal conductivity, and specific heat capacity of phantom, respectively. The objective function is defined by the degree of overlap between the model-predicted and observed ablation zones as such

$$\Omega = 1 - \frac{N_{\text{TP}}}{N_{\text{TP}} + N_{\text{FP}} + N_{\text{FN}}}, \quad (10)$$

where  $\Omega$  signifies the ratio of the intersection and union of the model-predicted and observed ablation zones. For this framework, we use the Nelder–Mead downhill simplex method to optimize the parameter set [Eq. (9)] by minimizing the objective function [Eq. (10)]. The Nelder–Mead algorithm is a heuristic search approach used to solve nonlinear optimization problems without requiring derivative information.

## 2.5 Agar-Albumin Hepatic Deformation Phantom

The deformable hepatic phantom used in this study consisted of a combination of purified water, 1.5 wt. % agar-agar powder (Thermo Fischer Scientific, Waltham, Massachusetts), and 50 wt. % liquid egg whites (Break Free Liquid Egg Whites, The Kroger Company, Cincinnati, Ohio). Liquid egg whites were used to produce a permanent visual history of the thermal induced ablation lesion, similar in nature to the ablation lesions that form in tissue. Egg whites contain around 10% ovalbumin protein dissolved in 90% water with nearly no carbohydrate or fat content. Thermal denaturing of the ovalbumin protein leads to aggregation, which causes optical scattering and a large reduction in the  $T_2$  relaxation coefficient of the material. The resulting ablation lesions were imaged using  $T_2$ -weighted MRI and visually observed with mock gross pathology by sectioning the phantom along the midline of the ablation antenna and backlighting the section [as seen in Figs. 1(b) and 1(c)].

To create the phantom, powdered agar-agar was thoroughly mixed with water and heated to boiling on a hot plate while being continuously stirred to produce a 1.5% agar gel. The solution was then cooled to <60°C with continuous stirring before adding the liquid egg whites. This cooling ensured that no protein denatured prematurely. The mixture was then mixed for 1 min and then poured into the phantom mold to allow the gel to set. A plaster negative derived from contrast-enhanced CT imaging of a patient liver was used as the phantom mold

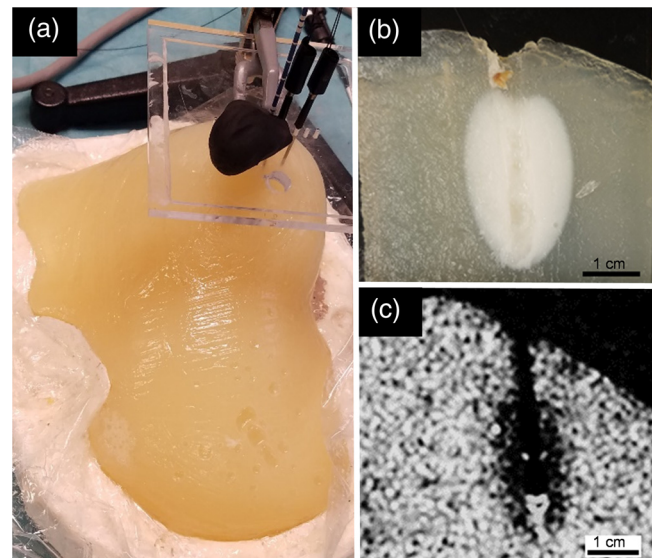


**Fig. 1** (a) Agar-albumin phantom liver in its predeformation state. MWA antenna is seen inserted into the right lobe. (b) Mock gross pathology of an ablation within the agar-albumin phantom. The outer ablation contour, ablation antenna tip location, and ablation antenna shaft are clearly visible. (c) Slice from the  $T_2$ -weighted MRI of the ablation zone from which the outer ablation contour, ablation antenna tip location, and ablation antenna shaft were segmented.

to produce a hepatic phantom with clinically relevant anatomical structure (Fig. 1).

## 2.6 Applied Deformations

The proposed modeling and registration framework was evaluated across a range of clinically relevant organ deformations. With respect to open surgery, deformations occur due to the introduction of packing material beneath and around the organ following mobilization of the organ from surrounding anatomy. With respect to intervention, changes between diagnostic and intraoperative presentation incur shape change. To impose soft tissue deformations, silicone support blocks (roughly 20 to 30 mm thick) were inserted beneath varying areas of the phantom to simulate surgical packing for organ presentation in the case of ablation under open surgical procedures. Figure 2 provides an example of the extent of deformation induced in the phantom. In total, four unique applications of deformation were applied to the phantom. In case 1, support material was placed beneath the lateral superior right lobe, raising the largest volume of the phantom. In case 2, support material was added beneath both the lateral superior and inferior right lobe, causing the right lobe to rise and rotate about the falciform ligament. In case 3, support material was inserted beneath the lateral inferior right lobe and the left lobe, causing the medial area of the liver to sag. Finally, in case 4, support material was inserted beneath the lateral inferior right lobe, causing it to rise. It should be noted that the distribution of signed closest point differences is similar to those that have been measured in the literature. More specifically, in Ref. 54, laser range data of the anterior surface were rigidly registered to the preoperative imaged counterpart and demonstrated this periodic distribution of signed closest point distances similar to Fig. 2. In addition, this was also seen in the analysis by Heiselman et al.<sup>27</sup> for the laparoscopic configuration.

## 2.7 Data Collection

T<sub>2</sub>-weighted MRI scans were acquired for each state of phantom deformation (i.e., one predeformation image set and four

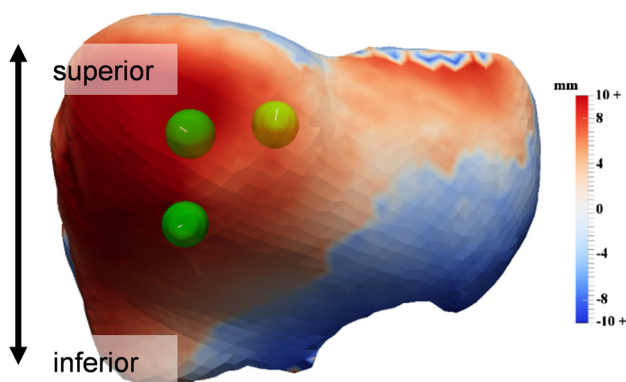


**Fig. 2** Representation of the degree of deformation achieved in the deformable hepatic ablation phantom. The colormap represents the signed surface error after rigidly registering the pre- and postdeformation phantom image segmentations. The ablation zones are presented as green volumes. In this case of deformation, 20- to 30-mm thick support material was placed beneath the superior right lobe to simulate surgical packing for organ presentation. In total, four applications of deformation were applied and imaged within the phantom.

post-deformation image sets). 3-D models were generated from each set of images using ITK-SNAP.<sup>55</sup> Salient feature regions were manually designated from the surface of each model. To date, these image-to-physical registration methods have been clinically implemented using sparse digitizations of the anterior organ surface attained intraoperatively. Within this study, we present and compare results following registration using (1) full-surface data, (2) sparse-surface data, and (3) resampled sparse-surface data using the resampling method presented by Collins et al.<sup>29</sup>

Sparse anterior surface data, akin to what would be available clinically, were generated using a method similar to the human-to-phantom data described by Collins et al.<sup>29</sup> Briefly, sparse-surface data gathered from actual clinical cases (an IRB approved study at Memorial Sloan Kettering Cancer Center in Ref. 28) were rigidly registered to our phantom image volume in its deformed state. This was accomplished using the weighted salient feature registration method of Clements et al.<sup>43</sup> Once initialized, an affine registration was performed to account for any differences in organ size between the clinical and phantom data. Next, the clinical surface data were projected to their closest points on the deformed phantom surface, resulting in unique realistic sparse anterior surface designations for each case. However, unlike the method of Collins et al.,<sup>29</sup> no additional noise was added to these synthesized sparse-surface data. All synthesized designations had an extent of organ coverage between 25% and 30%, which is within the range of typical clinical data acquisition.<sup>27,56</sup> It should be noted that the above process could be performed in the reciprocal workflow allowing for a second set of novel conditions (i.e., treating the actual “postdeformation” data as the preoperative organ state and the actual “predeformation” data as the intraoperative organ state). In total, this created eight registration scenarios (the original four cases from Sec. 2.6 and the four reciprocal instances) for the results herein, each with an independent set of simulated physical space data to drive the registrations.

## 2.8 Analysis

Two methods of image-to-physical registration were compared in this study: (1) the salient feature weighted iterative closest point rigid registration method by Clements et al.<sup>43</sup> and (2) the deformable control point nonrigid registration method by Heiselman et al.<sup>27</sup> Average target registration error (TRE) was used as the primary quantification of registration accuracy. A total of nine targets were measured across the three ablations in each image-to-physical registration scenario: (a) the antenna tip locations, (b) the antenna insertion points on the phantom surface, and (c) the centroids of the MRI-segmented ablation zones. Average TRE for a registration scenario was calculated as the average distance between corresponding points in the registered image and physical data sets. This metric measures the accuracy of the registration methods evaluated in this study exclusively, independent of the MWA modeling.

The positive predictive value (PPV) was used to evaluate volumetric accuracy of the predictive MWA model. PPV was calculated as

$$\text{PPV} = \frac{N_{\text{TP}}}{N_{\text{TP}} + N_{\text{FP}}}, \quad (11)$$

where  $N_{\text{TP}}$  is the volume of the model-predicted ablation zone overlapping with the observed ablation zone and  $N_{\text{FP}}$  is the

volume of the model-predicted ablation zone, which does not overlap with the true ablation zone. We present the metric of PPV in this study for two separate purposes: (1) to quantify the predictive capability of the MWA model without compounding registration error and (2) to evaluate the accuracy of the combined registration and MWA modeling framework.

To singularly evaluate the accuracy of the MWA model, the model-predicted ablation zones were directly compared to the mock gross pathology. This comparison was made assuming perfect registration after manually aligning the ablation antenna tip and shaft from the model space with the corresponding locations in the mock gross pathology image space. The outer ablation contours from each space were then revolved to create 3-D volumes, which were then compared by calculating the PPV. The combined registration and modeling framework accuracy was also evaluated by computing the PPV following registration of the model-predicted ablation zone. Inaccuracies in both the image-to-physical registration methods and MWA modeling contribute to the error encompassed by this metric.

The Wilcoxon rank sum test was used to determine significance in differences between the distributions of TRE and PPV resulting from each ablation (i.e., 24 total) and each evaluated registration method ( $\alpha = 0.05$ ).

### 3 Results

#### 3.1 Microwave Ablation Model

Model-predicted temperature maps for each of the three ablations with the agar-albumin deformation phantom are presented in Fig. 3 alongside contours defining the observed and model-predicted ablation zone extents (as black and dashed red lines, respectively). These results are under the condition of perfect localization, which was achieved by manually aligning the observed and modeled ablation antennas. The degree of ablation zone overlap for this condition is presented as the PPV, averaging  $96.3 \pm 0.3\%$ . The observed transverse and axial ablation zone dimensions gathered from mock gross pathology were  $20.1 \pm 1.0$  and  $31.6 \pm 1.2$  mm, respectively. Model-predicted

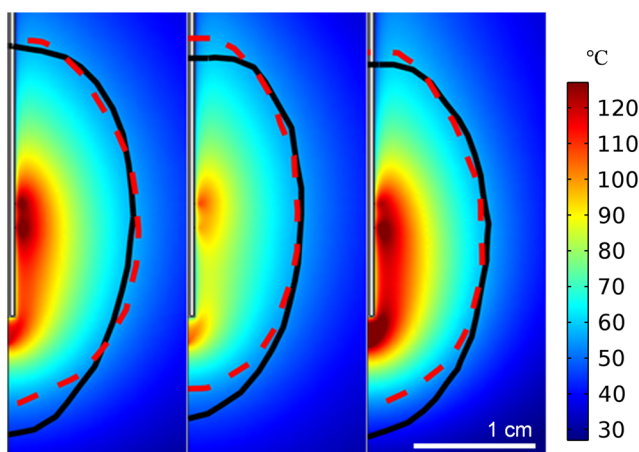


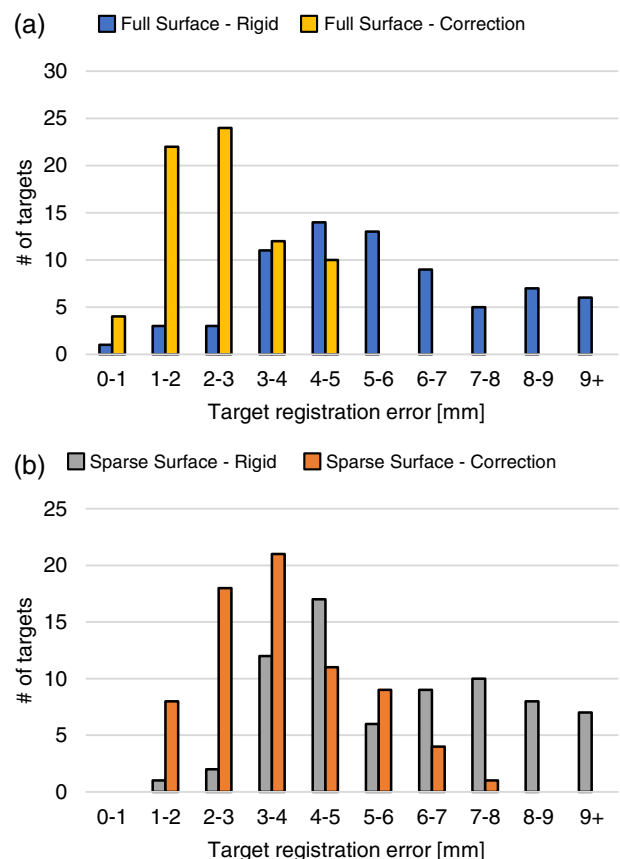
**Fig. 3** Model-predicted temperature maps, observed (black line), and model-predicted (red dashed line) ablation zones are presented for each case of ablation with the Perseon ST antenna within the agar-albumin hepatic deformation phantom. The observed ablation zone extent was gathered from mock gross pathology and used to drive the inverse MWA model. It is important to note that each ablation occurred in a different area of the phantom with varying tissue thickness and antenna depth.

ablation zone transverse and axial dimensions were  $19.9 \pm 1.8$  and  $29.9 \pm 0.6$  mm, respectively (differing from the mock gross pathology by 4.2% and 5.3%, respectively).

#### 3.2 Image-to-Physical Registration

TREs resulting from rigid registration and deformation correction approaches applied to the eight registration scenarios within the deformable hepatic ablation phantom are presented in Fig. 4 for full-surface data (top) and sparse-surface data (bottom), in blue/yellow and gray/orange, respectively. Average TRE results from driving the registrations with full-surface, sparse-surface, and resampled sparse-surface data are tabulated for both methods of registration in Table 1.

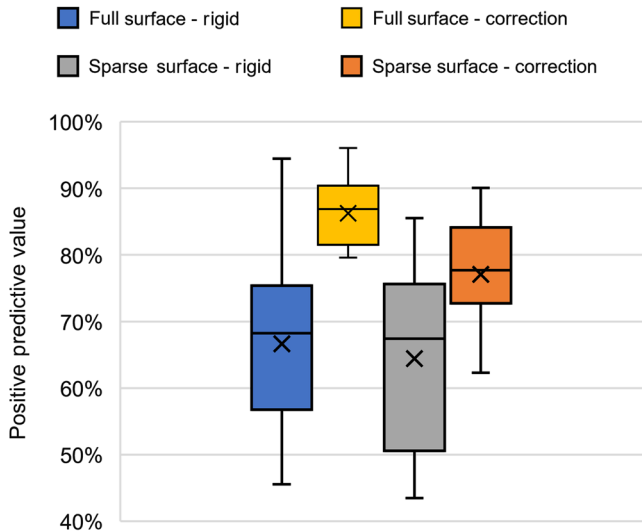
Distributions of the volumetric overlap (represented by PPV) resulting from the rigid registration and deformation correction methods using full and sparse-surface data are shown in Fig. 5 in blue/yellow (full data) and gray/orange (partial data), respectively. Average PPV results from driving the registrations with full-surface, sparse-surface, and resampled sparse-surface data are presented for both methods of registration in Table 2. Figure 6 presents the PPV plotted as a function of the average TRE for the corresponding ablation antenna for each method of registration as well as for the perfectly localized model



**Fig. 4** Histograms of the target errors resulting from the two methods of registration applied to the eight image-to-physical registration scenarios within our agar-albumin deformation phantom. Results of the rigid registration using the weighted salient feature ICP method of Clements et al.<sup>43</sup> are presented in blue/gray. Results of the deformation correction method of Heiselman et al.<sup>27</sup> are presented in yellow/orange. (a) Results from registering with full-surface data. (b) Results from registering with sparse-surface data.

**Table 1** Average and standard deviation TRE are presented for each source of surface data and each evaluated method of registration.

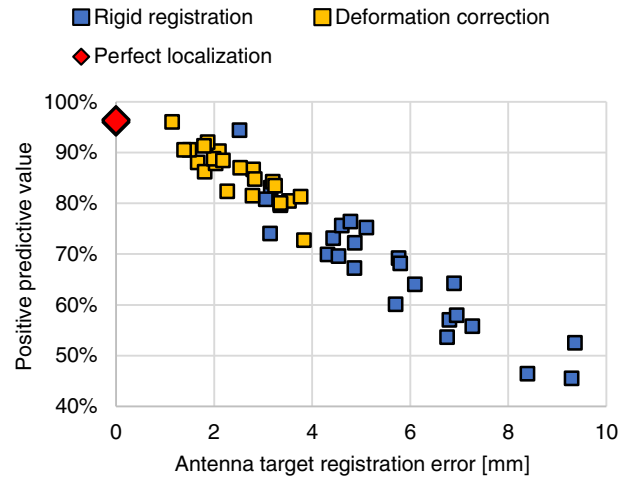
Surface data	Average TRE (mm)	
	Rigid registration	Deformation correction
Full	5.6 ± 2.3	2.5 ± 1.1
Sparse	6.0 ± 2.3	3.7 ± 1.4
Resampled	4.9 ± 2.1	3.8 ± 1.3

**Fig. 5** Distributions of the volumetric overlap of observed and predicted ablation zones represented by the PPV. The box and whiskers represent the mean, median, upper and lower quartiles, maximum, and minimum PPV for the rigid registration method of Clements et al.<sup>43</sup> in blue/gray and the deformation correction method of Heiselman et al.<sup>27</sup> in yellow/orange. Presented results are from registering with full-surface data (blue/yellow) and sparse-surface data (gray/orange).**Table 2** Average and standard deviation volumetric overlap are presented as the PPV for each source of surface data and each evaluated method of registration. Additionally, the PPV is presented for the case of perfect localization to distinguish model error from registration error.

Surface data	Average PPV (%)	
	Rigid registration	Deformation correction
Full	67.0 ± 11.8	85.6 ± 5.0
Sparse	64.8 ± 12.4	77.1 ± 8.0
Resampled	69 ± 11.1	75.1 ± 6.5
Perfect localization	96.3 ± 0.3	

(i.e., TRE of 0 mm). Results shown in Fig. 6 are from driving the registration methods with full-surface data.

Figure 7 presents an example of the retrospective ablation model following rigid registration and deformation correction using sparse anterior surface data. In each panel, the green

**Fig. 6** The PPV is presented for each registered ablation (24 total) as a function of the average target registration of the corresponding ablation antenna. Antenna TRE was calculated as the average error of the antenna tip, insertion point, and ablation centroid. Results of the rigid registration method of Clements et al.<sup>43</sup> are presented in blue and the deformation correction method of Heiselman et al.<sup>27</sup> are presented in yellow. MWA model results in the condition of perfect registration (manual alignment) are presented for comparison in red. Presented results are from registering with full-surface data.

ellipse and line represent the ground truth ablation zone and antenna pose, respectively. The modeled ablation zone following rigid registration is presented in (a) and magnified in (b). The MWA model result following deformation correction is presented in (c) and magnified in (d).

## 4 Discussion

While the impact of soft-tissue deformation on thermal development has been explored in other contexts,<sup>57</sup> with this work, we present the first effort to evaluate deformation correction methods for image-guided hepatic MWA in the open surgical setting. Further, we couple a simple retrospective model of the ablation procedure with clinically relevant image-guidance techniques, allowing for a greater understanding of the magnitude of error that can be associated with a combined modeling and surgical navigation approach. We evaluate these methods within a deformable hepatic ablation phantom that allows for comprehensive validation with both individual point targets and volumetric overlap of predicted and ground-truth ablation zones.

The example visualization of the evaluated registration algorithms on ablation antenna localization (Fig. 7) tangibly demonstrates the degree to which the applied deformation correction method is an improvement upon the rigid registration when soft-tissue deformation is present. This result is further supported by the quantitative results of the ablation antenna target errors in Fig. 4 and Table 1, indicating that the deformable registration method of Heiselman et al.<sup>27</sup> represented a significant improvement over the rigid registration results of Clements et al.<sup>43</sup> ( $p < 0.001$ ). Additionally, these results demonstrate that a more complete source of surface data (e.g., as can be available in a CBCT-assisted percutaneous ablation procedure) for driving the registration provides further improvement to the correction when compared to the sparse-surface data that is available in the open setting ( $p < 0.001$ ). From these results, it is also interesting to note that the source of surface data has a much more pronounced impact on the deformation correction method than

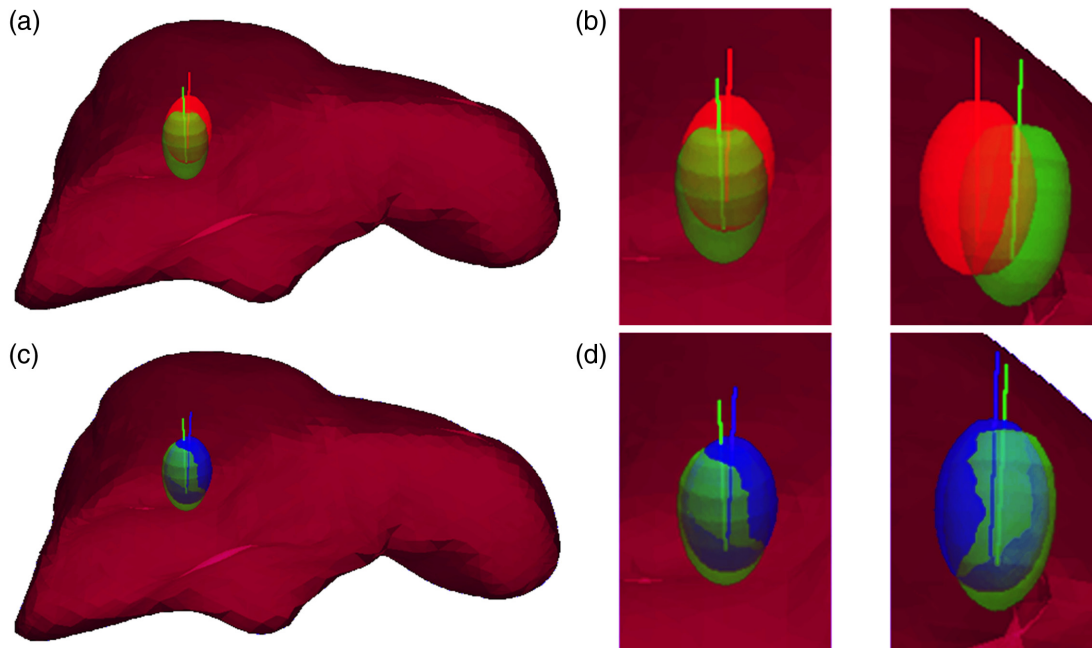


**Fig. 7** An example of ablation model predictions following registration with sparse anterior surface data. In each panel, green represents the ground truth ablation zone as observed in MRI. The rigidly registered ablation model is presented in (a) and detailed views in (b). The registered ablation model following deformation correction is presented in (c) and detailed views in (d). Additionally, in each panel the registered ablation antenna are indicated by lines with color corresponding to the registration method.

on the rigid registration. We interpret this result to be a representation of the degree to which soft-tissue deformation impacts the maximum achievable accuracy of rigid registration approaches within this setting. We also note that the relatively low rigid registration errors achieved in this study, as compared to prior phantom studies, indicate that the degree of achieved soft-tissue deformation within the phantom was achieved in a previous study.<sup>26</sup> We believe that this is in large part due to the nature of the agar-albumin phantom, which is prone to shearing when subjected to very large deformations. However, from our past characterizations, we suggest that the 20 to 30 mm of deformation that was achieved in this study was representative of clinical use and was adequate for understanding the relative performance of the registration methods.<sup>27,54</sup> Additionally, while the resampled sparse-surface data provide further improvement to the rigid registration method, that was not the case for the deformation correction method as it was in original 2017 study.<sup>29</sup> We believe that this is because the simulated sparse-surface data in this work did not include simulated acquisition noise (i.e., it was selected directly from the MRI surface), which the resampling approach was specifically designed to address (e.g., we have observed manually swabbed organ surface data to have an average noise of 1 to 2 mm).

In addition to reporting antenna target errors, the volumetric error associated with the retrospectively modeled ablation zones has been presented in Fig. 5 and Table 2. Again, these results demonstrate improved localization by the deformation correction method. This is clearly demonstrated in Fig. 7 when comparing the overlap of the red ablation (rigid registration) with the green (ground-truth) to the overlap of the blue ablation (deformation corrected) on the same ground-truth. As with the target errors, we see in Table 2 that for each data source the deformation correction method of Heiselman et al.<sup>27</sup> significantly improves upon the rigid alignment method of Clements

et al.<sup>43</sup> ( $p < 0.001$ ). These registration results are in line with previous clinical and phantom evaluations.<sup>27,28,30</sup>

Figure 3 and Table 2 present the maximum volumetric accuracy of the retrospective ablation model under the condition of perfect localization. Furthermore, Fig. 6 presents these results in comparison to the modeled ablation zones following registration as a function of their localization accuracy. These novel results represent the loss in model-predictive capacity ( $-5.95\%/mm$ ,  $p < 0.001$ ,  $r = 0.93$ ) that is associated with increasing antenna localization error in a combined navigation and modeling framework. However, in this initial work, we retrospectively model the ablation outcome by reconstructing phantom-specific properties, which limit immediate clinical applicability. Although, there is precedence within the literature for determining disease state and approximating tissue properties from preoperative imaging using MRI<sup>58</sup> or ultrasound.<sup>59</sup> Another limitation to the current model is that neither the phantom nor the model include tissue perfusion, which has been shown to have an impact on ablation outcome<sup>43-47</sup> but is difficult to implement within the phantom setting.

Further development of these methods would provide a platform for clinicians to preoperatively define an approach for ablating targeted lesions while sparing healthy tissue and ensuring adequate margins. Such a patient-specific plan would provide ablation antenna target and trajectory information that would then be provided intraoperatively to achieve the optimal ablation. During treatment, organ surface data would be collected and then used to achieve a deformable registration using the methods presented in this work. Finally, under enhanced image-guidance, the physician could then deploy the ablation antenna to the preoperatively defined configuration, confirming placement with tracked iUS, before delivery therapy.

In summary, our results suggest that this application is a significant advancement in the field of open hepatic image-guided

ablation, as soft-tissue deformation is a considerable limitation to current modeling and guidance frameworks for liver tumor treatments.<sup>57</sup> While EM-iUS methods<sup>18,19</sup> take a purely intraoperative imaging approach to this soft-tissue deformation problem, they fail to provide additional information concerning relevant critical anatomy, a common desire given the availability of preoperative imaging data. Furthermore, EM-iUS approaches are restricted to US-visible tumors, which restrict its applicability when considering nonechogenic tumors that can present following neoadjuvant therapy.<sup>22,23</sup> Other studies have reported targeting accuracy of ablation antennas on the order of 5 to 10 mm, with the current best being a median accuracy of 4.2 mm.<sup>19</sup> In comparison, our presented method of deformation correction has produced favorable accuracies of  $2.5 \pm 1.1$  and  $3.7 \pm 1.4$  mm when using full- and sparse-surface data, respectively. While this work was directed toward the open surgical setting, we show that these methods can enhance image-guidance for percutaneous, laparoscopic, and open hepatic ablation procedures.

## 5 Conclusions

The objective of this work was to quantify the localization and volumetric accuracy of a model-based deformation correction method when applied to image-guided hepatic MWA. Evaluation of the applied method shows significant improvement in localization accuracy when compared to a clinically relevant rigid registration approach. Furthermore, we incorporate a simple, retrospective model of MWA into the navigational framework, providing an important initial evaluation of the interplay between localization accuracy and volumetric overlap of predicted and ground-truth ablation zones. While future work is necessary to apply this modeling and navigational framework as a prospective, targeting approach, the deformation correction method applied in this study is certainly an advancement toward improved localization in open hepatic MWA procedures. Going further, this work proposes to extend the concept of “model correction” in surgical navigation to include a new biophysical domain, namely the deposition of ablative energy, and its corresponding thermal evolution. This combined mechanics/energy framework represents the first study toward a more comprehensive model-predictive paradigm for an important image-guided therapeutic process in use today.

## Disclosures

The authors declare that they have no disclosures or conflicts of interest.

## Acknowledgments

This work was supported by the National Institutes of Health with awards R01CA162477 from the National Cancer Institute and T32EB021937 from the National Institute of Biomedical Imaging and Bioengineering.

## References

- R. C. G. Martin, C. R. Scoggins, and K. M. McMasters, “Safety and efficacy of microwave ablation of hepatic tumors: a prospective review of a 5-year experience,” *Ann. Surg. Oncol.* **17**, 171–178 (2010).
- C. Correa-Gallego et al., “A retrospective comparison of microwave ablation vs. radiofrequency ablation for colorectal cancer hepatic metastases,” *Ann. Surg. Oncol.* **21**(13), 4278–4283 (2014).
- T. A. Potretzke et al., “Microwave versus radiofrequency ablation treatment for hepatocellular carcinoma: a comparison of efficacy at a single center,” *J. Vasc. Interventional Radiol.* **27**(5), 631–638 (2016).
- L. Solbiati et al., “Percutaneous radio-frequency ablation of hepatic metastases from colorectal cancer: long-term results in 117 patients,” *Radiology* **221**(1), 159–166 (2001).
- N. V. Violi et al., “Efficacy of microwave ablation versus radiofrequency ablation for the treatment of hepatocellular carcinoma in patients with chronic liver disease: a randomized controlled phase 2 trial,” *Lancet Gastroenterol. Hepatol.* **3**(5), 317–325 (2018).
- U. Leung et al., “Long-term outcomes following microwave ablation for liver malignancies,” *Br. J. Surg.* **102**, 85–91 (2015).
- C. Simon, D. E. Dupuy, and W. W. Mayo-Smith, “Microwave ablation: principles and applications,” *Radiographics* **25**, S69–S83 (2005).
- I. R. Andersen et al., “Long-term survival following ablation of colorectal liver metastases,” *J. Surg.* **6**, 13–18 (2018).
- R. P. DeMatteo et al., “Anatomic segmental hepatic resection is superior to wedge resection as an oncologic operation for colorectal liver metastases,” *J. Gastrointest. Surg.* **4**(2), 178–184 (2000).
- T. Ikemoto, M. Shimada, and S. Yamada, “Pathophysiology of recurrent hepatocellular carcinoma after radiofrequency ablation,” *Hepatol. Res.* **47**, 23–30 (2016).
- R. S. Winokur et al., “Characterization of in vivo ablation zones following percutaneous microwave ablation of the liver with two commercially available devices: are manufacturer published reference values useful?” *J. Vasc. Interventional Radiol.* **25**(12), 1939–1946.e1 (2014).
- D. T. Glidden et al., “Clinically observed ablation volumes as compared to vendor specified volumes: the emperor’s new clothes,” *J. Vasc. Interventional Radiol.* **25**(3), S76 (2014).
- T. P. Kingham et al., “Image-guided liver surgery, intraoperative projection of computed tomography images utilizing tracked ultrasound,” *HPB* **14**(9), 594–603 (2012).
- R. C. G. Martin and D. A. North, “Enhanced ultrasound with navigation leads to improved liver lesion identification and needle placement,” *J. Surg. Res.* **200**(2), 420–426 (2016).
- D. Sindram et al., “Real-time three-dimensional guided ultrasound targeting system for microwave ablation of liver tumours: a human pilot study,” *HPB* **13**(3), 185–191 (2011).
- V. M. Banz et al., “Intraoperative image-guided navigation system: development and applicability in 65 patients undergoing liver surgery,” *Langenbeck’s Arch. Surg.* **401**, 495–502 (2016).
- C. W. Hammill et al., “Evaluation of a minimally invasive image-guided surgery system for hepatic ablation procedures,” *Surg. Innov.* **21**(4), 419–426 (2014).
- D. Sindram et al., “Laparoscopic microwave ablation of human liver tumours using a novel three-dimensional magnetic guidance system,” *HPB* **17**, 87–93 (2015).
- I. Paolucci et al., “Design and implementation of an electromagnetic ultrasound-based navigation technique for laparoscopic ablation of liver tumors,” *Surg. Endosc.* **32**, 3410–3419 (2018).
- P. Tinguely et al., “Laparoscopic image-based navigation for microwave ablation of liver tumors: a multi-center study,” *Surg. Endosc.* **31**, 4315–4324 (2017).
- D. J. Hawkes et al., “Tissue deformation and shape models in image-guided interventions: a discussion paper,” *Med. Image Anal.* **9**(2), 163–175 (2005).
- A. Irshad, M. Anis, and S. J. Ackerman, “Current role of ultrasound in chronic liver disease: surveillance, diagnosis and management of hepatic neoplasms,” *Curr. Prob. Diagn. Radiol.* **41**, 43–51 (2012).
- T. P. Kingham et al., “3D image guidance assisted identification of colorectal cancer liver metastases not seen on intraoperative ultrasound: results from a prospective trial,” *HPB* **20**(3), 260–267 (2018).
- T. Lange et al., “Vessel-based non-rigid registration of MR/CT and 3D ultrasound for navigation in liver surgery,” *Comp. Aided Surg.* **8**(5), 228–240 (2003).
- Y. Hu et al., “Deformable vessel-based registration using landmark-guided coherent point drift,” *Lect. Notes Comput. Sci.* **6326**, 60–69 (2010).
- D. C. Rucker et al., “A mechanics-based nonrigid registration method for liver surgery using sparse intraoperative data,” *IEEE Trans. Med. Imaging* **33**, 147–158 (2014).

27. J. S. Heiselman et al., "Characterization and correction of intraoperative soft tissue deformation in image-guided laparoscopic liver surgery," *J. Med. Imaging* **5**(2), 021203 (2017).
28. L. W. Clements et al., "Evaluation of model-based deformation correction in image-guided liver surgery via tracked intraoperative ultrasound," *J. Med. Imaging* **3**, 015003 (2016).
29. J. A. Collins et al., "Improving registration robustness for image-guided liver surgery in a novel human-to-phantom data framework," *IEEE Trans. Med. Imaging* **36**(7), 1502–1510 (2017).
30. L. W. Clements et al., "Deformation correction of image guided liver surgery: an intraoperative fidelity assessment," *Surgery* **162**(3), 537–547 (2017).
31. L. Ludemann et al., "Non-invasive magnetic resonance thermography during regional hyperthermia," *Int. J. Hyperther.* **26**(3), 273–282 (2010).
32. E. S. Ebbini, C. Simon, and D. Liu, "Real-time ultrasound thermography and thermometry," *IEEE Signal Process. Mag.* **35**(2), 166–174 (2018).
33. G. Deshazer et al., "Computational modelling of 915 MHz microwave ablation: comparative assessment of temperature-dependent tissue dielectric models," *Med. Phys.* **44**(9), 4859–4868 (2017).
34. Z. Ji and C. L. Brace, "Expanded modelling of temperature-dependent dielectric properties for microwave thermal ablation," *Phys. Med. Biol.* **56**(16), 5249–5264 (2011).
35. D. Liu and C. L. Brace, "Numerical simulation of microwave ablation incorporating tissue contraction based on thermal dose," *Phys. Med. Biol.* **62**(6), 2070–2086 (2017).
36. C. Rossmann and D. Haemmerich, "Review of temperature dependence of thermal properties, dielectric properties, and perfusion of biological tissues at hyperthermic and ablation temperatures," *Crit. Rev. Biomed. Eng.* **42**(6), 467–492 (2014).
37. D. Yang et al., "Measurement and analysis of tissue temperature during microwave liver ablation," *IEEE Trans. Biomed. Eng.* **54**, 150–155 (2007).
38. D. Haemmerich et al., "Hepatic bipolar radiofrequency ablation creates coagulation zones close to blood vessels: a finite element study," *Med. Biol. Eng. Comput.* **41**(3), 317–323 (2003).
39. W. Schramm, D. Yang, and D. Haemmerich, "Contribution of direct heating, thermal conduction and perfusion during radiofrequency and microwave ablation," in *Int. Conf. IEEE Eng. Med. and Biol. Soc.*, New York (2006).
40. N. C. Yu et al., "Microwave liver ablation: influence of hepatic vein size on heat-sink effect in a porcine model," *J. Vasc. Interventional Radiol.* **19**(7), 1087–1092 (2008).
41. A. Marengo, C. Rosso, and E. Bugianesi, "Liver cancer: connections with obesity, fatty liver, and cirrhosis," *Annu. Rev. Med.* **67**, 103–117 (2016).
42. A. P. O'Rourke et al., "Dielectric properties of human normal, malignant and cirrhotic liver tissue: in vivo and ex vivo measurements from 0.5 to 20 GHz using a precision open-ended coaxial probe," *Phys. Med. Biol.* **52**(15), 4707–4719 (2007).
43. L. W. Clements et al., "Robust surface registration using salient anatomical features for image-guided liver surgery: algorithm and validation," *Med. Phys.* **35**(6), 2528–2540 (2008).
44. L. W. Clements et al., "Organ surface deformation measurement and analysis in open hepatic surgery: method and preliminary results from 12 clinical cases," *IEEE Trans. Biomed. Eng.* **58**(8), 2280–2289 (2011).
45. D. A. Gervais et al., "Society of interventional radiology position statement on percutaneous radiofrequency ablation for the treatment of liver tumors," *J. Vasc. Interventional Radiol.* **20**(7), S342–S347 (2009).
46. A. Gillams et al., "Thermal ablation of colorectal liver metastases: a position paper by an international panel of ablation experts, the interventional oncology sans Frontières meeting 2013," *Eur. Radiol.* **25**(12), 3438–3454 (2015).
47. R. S. Puijk et al., "Percutaneous liver tumour ablation: image guidance, endpoint assessment, and quality control," *Can. Assoc. Radiol. J.* **69**(1), 51–62 (2018).
48. J. Iwazawa et al., "Ablation margin assessment of liver tumors with intravenous contrast-enhanced C-arm computed tomography," *World J. Radiol.* **4**(3), 109–114 (2012).
49. R. L. Cazzato et al., "Flat-panel cone-beam CT-guided radiofrequency ablation of very small ( $\leq 1.5$  cm) liver tumors: technical note on a preliminary experience," *Cardiovasc. Interventional Radiol.* **38**(1), 206–212 (2015).
50. M. Abdel-Rehim et al., "Assessment of liver ablation using cone beam computed tomography," *World J. Gastroenterol.* **21**(2), 517–524 (2015).
51. M. Morimoto et al., "C-arm cone beam CT for hepatic tumor ablation under real-time 3D imaging," *AJR Am. J. Roentgenol.* **194**(5), W452–W454 (2010).
52. N. Abi-Jaoudeh et al., "Clinical experience with cone-beam CT navigation for tumor ablation," *J. Vasc. Interventional Radiol.* **26**(2), 214–219 (2015).
53. C. Floridi et al., "Clinical impact of cone beam computed tomography on iterative treatment planning during ultrasound-guided percutaneous ablation of liver malignancies," *Med. Oncol.* **34**, 113 (2017).
54. COMSOL Inc., *COMSOL Multiphysics Reference Manual*, COMSOL Inc., Burlington, Massachusetts (2013).
55. P. A. Yushkevich et al., "User-guided 2D active contour segmentation of anatomical structures: significantly improved efficiency and reliability," *Neuroimage* **31**(3), 1116–1128 (2006).
56. R. Plantefeve et al., "Patient-specific biomechanical modeling for guidance during minimally-invasive hepatic surgery," *Ann. Biomed. Eng.* **44**, 139–153 (2016).
57. E. J. Rijkhorst et al., "Effects of respiratory liver motion on heating for gated and model-based motion compensated high-intensity focused ultrasound ablation," *Lect. Notes Comput. Sci.* **6891**, 605–612 (2011).
58. V. Bhat et al., "Quantification of liver fat with mDIXON magnetic resonance imaging, comparison with the computed tomography and the biopsy," *J. Clin. Diagn. Res.* **11**(7), TC06–TC10 (2017).
59. Y. Fujiwara et al., "The b-mode image-guided ultrasound attenuation parameter accurately detects hepatic steatosis in chronic liver disease," *Ultrasound Med. Biol.* **44**(11), 2223–2232 (2018).

Biographies of the authors are not available.